Materials Today Nano 22 (2023) 100316

Contents lists available at ScienceDirect

Materials Today Nano

journal homepage: https://www.evise.com/profile/#/MTNANO/login

Anisotropic optical and magnetic response in self-assembled TiN–$CoFe_2$ nanocomposites

J. Song [a], Di Zhang [a, b], P. Lu [c], H. Wang [d], X. Xu [d], M.L. Meyerson [c], S.G. Rosenberg [c], J. Deitz [c], J. Liu [a], X. Wang [b], X. Zhang [a], H. Wang [a, e, *]

[a] School of Materials Engineering, Purdue University, West Lafayette, 47907, USA
[b] Center for Integrated Nanotechnologies (CINT), Los Alamos National Laboratory, Los Alamos, NM 87545, USA
[c] Sandia National Laboratories, Albuquerque, NM 87185, USA
[d] Department of Physics and Astronomy, University of Nebraska-Lincoln, Lincoln, NE 68588, USA
[e] School of Electrical and Computer Engineering, Purdue University, West Lafayette, 47907, USA

ARTICLE INFO

Article history:
Received 6 October 2022
Received in revised form
12 January 2023
Accepted 25 January 2023
Available online 2 February 2023

Keywords:
Vertically aligned nanocomposites
Tunable microstructure
Hyperbolic metamaterial
Magnetic anisotropy
Magneto-optical coupling

ABSTRACT

Transition metal nitrides (e.g., TiN) have shown tremendous promise in optical metamaterials for nanophotonic devices due to their plasmonic properties comparable to noble metals and superior high temperature stability. Vertically aligned nanocomposites (VANs) offer a great platform for combining two dissimilar functional materials with a one-step deposition technique toward multifunctionality integration and strong structural/property anisotropy. Here, we report a two-phase nanocomposite design combining ferromagnetic $CoFe_2$ nanosheets in the plasmonic TiN matrix as a new hybrid plasmonic metamaterial. The hybrid metamaterials exhibit anisotropic optical and magnetic responses, as well as a pronounced magneto-optical coupling response evidenced by Magneto-optic Kerr Effect measurement, owing to the novel vertically aligned structure. This work demonstrates a new TiN-based metamaterial with anisotropic properties and multifunctionality toward light polarization modulation, optical switching, and integrated optics.

1. Introduction

Optical metamaterials consist of artificially designed nanostructured materials which generate unique optical properties that are not exhibited in natural materials. These novel optical properties, including negative refractive index [1,2], near-zero-index [3], and hyperbolic dispersion [4,5] and originate from the confinement of light propagation in nanostructured materials. Noble metals (e.g., Au and Ag) are widely used in forming nanostructured plasmonic metamaterials due to their strong surface plasmon resonance. However, plasmonic metals exhibit high optical loss in the visible to near-infrared (vis-NIR) region due to interband and intraband transitions [6]. In addition, other challenges in terms of fabrication and integration, as well as permittivity tuning of plasmonic metamaterials, greatly hinder their performances and applications [7]. Therefore, seeking alternative plasmonic materials is necessary to overcome these drawbacks. Transition metal nitrides (e.g., TiN, TaN, ZrN) are promising candidates for plasmonic applications because of their metallic response in most optical wavelengths and high structural stability. Tailoring stoichiometry in nitrides allows tuning of optical properties easily [8]. Considering the fabrication and integration challenges of metals, transition metal nitrides are compatible with the complementary metal-oxide-semiconductor process and can be easily integrated on various substrates (e.g., MgO, STO, Si, sapphire) [9,10]. Besides, the high mechanical strength and high melting temperature enable them to be promising materials for future high-temperature plasmonic applications [11,12].

With the development of nanofabrication techniques, various nanostructured nitrides have been demonstrated for plasmonic applications, for example, periodic array of TiN nanoparticles [13], nanoantennas [14], nanotrenchs [15], and nanorings [16]. The integration of TiN with dielectric materials (e.g., AlN, MgO) into a multilayer structure has been explored exhibiting hyperbolic dispersion [17,18]. However, most of these TiN-based metamaterials rely on high-cost fabrication techniques, including e-beam lithography and focused ion-beam process. Compared to the

* Corresponding author.
E-mail address: hwang00@purdue.edu (H. Wang).

https://doi.org/10.1016/j.mtnano.2023.100316

conventional fabrication methods, a cost-effective self-assembly approach to growing hybrid materials into a vertically aligned nanocomposites (VANs) form has recently attracted tremendous interest. Multiple two-phase nitride-metal nanocomposites [19–21], such as TaN–Au, TiN–Au, and TiN–Ag, have been successfully demonstrated in VANs with enhanced surface plasmon resonance and nonlinear optical responses. Taking advantage of these simple self-assembly VAN platforms, other nitride-based nanostructures can be further derived by additional processes. For example, TiN nanohole arrays have been achieved by selectively etching away the Au nanopillars from TiN–Au VANs [22], and a 3D plasmonic framework is formed by alternating TiN–Au and TaN–Au layers [23]. Most of the prior demonstrations have been focusing on nitride-metal [19–21] or oxide-metal [24–29] systems as hybrid metamaterials.

Another opportunity brought by the designs of VANs is integrating different functionalities in one material system. Functional materials are a large material family with a wide selection of properties, such as plasmonic (e.g., Au [7]), superconductivity (e.g., $YBa_2Cu_3O_{7-\delta}$ [30]), ferromagnetic (e.g., $CoFe_2O_4$ [31], $MnFe_2O_4$ [32], $CoFe_2$ [33]), ferroelectricity (e.g., $BaTiO_3$ [34]), and multiferroicity (e.g., $BiFeO_3$ [35]). Multifunctionality, as well as coupling effects, has been demonstrated in oxide-based VANs, such as magneto-electric coupling [36–38] and magneto-optic coupling effects [25,39,40]. On the other hand, most of the previous nitride-based VANs focus on incorporating plasmonic metal nanopillars toward optical tunability. Therefore, incorporating a secondary functional phase into the nitride matrix could enormously broaden the nitride VAN designs with other functionality. However, such nitride-based nanocomposite demonstration is very limited due to the challenges in material design incompatibility and differences in growth parameters required for the different phases.

In this work, we report a new hybrid metamaterial system of TiN-based nanocomposite with ferromagnetic $CoFe_2$ in the VAN form with strong anisotropic optical and magnetic properties. Here, ferromagnetic $CoFe_2$ nanopillars were formed by reducing $CoFe_2O_4$ in the target material during the high vacuum condition required by TiN growth. The TiN–$CoFe_2$ VANs are expected to exhibit optical and magnetic anisotropy as well as potential magneto-optical (MO) coupling. Laser frequency is varied to be 2 Hz and 10 Hz to effectively tune the dimension of $CoFe_2$ pillars. This demonstration shows the potential of designing new nitride-based VAN systems with multifunctionalities, property coupling, as well as effective property tunability.

2. Results and discussion

The microstructure of TiN–$CoFe_2$ nanocomposites thin films was first characterized by X-ray diffraction (XRD) analysis using θ-2θ scans as shown in Fig. S1. An out-of-plane of TiN (002) and MgO (002) can be clearly observed in the 2 Hz and 10 Hz deposited samples. The peak at the right side of the substrate MgO peak ($2\theta = 43.254^\circ$) can be identified as $CoFe_2$ (011). The out-of-plane d-spacing of CoFe2 (011) was determined by 2.09 Å, which is in 3.5% strain compared to its bulk value 2.02 Å. To reveal the detailed chemical distribution and 2-phase morphology in the system, a scanning transmission electron microscopy (STEM) analysis along with energy-dispersive X-ray spectroscopy (EDS) mapping was conducted on the samples in both cross-section and plan-view directions. As shown in the cross-sectional (Fig. 1b) and plan-view (Fig. 1d) STEM images, the two-phase nanocomposites exhibit a nanosheet-in-matrix structure. In the STEM images taken using the high angle annular dark field (HAADF) detector, the contrast is proportional to the atomic number (i.e., ~$Z^{1.7}$) [41–43]. Therefore, the brighter nanosheet region is related to the higher atomic number of Co (Z = 26) and Fe (Z = 27), compared to TiN (averaged Z = 14.5). The EDS maps in Fig. 1e further confirm the formation of ultrathin nanosheets made of Co and Fe, perpendicularly embedded in the TiN matrix. Furthermore, two high-resolution STEM images with higher magnifications from one of the nanosheet regions from the cross-sectional and plan-view images are shown in Fig. 1c and f respectively. Based on the lattices measured and symmetry identified, it determines that the nanosheets in the view area are metallic $CoFe_2$ with a body-center-cubic (bcc) structure and a lattice constant of 2.86 Å and furthermore form an epitaxy with the TiN matrix.

Of additional interest is that the "pillars" shape is rectangular in-plane (shown in plan-view images Fig. 1d–f), that is, thin sheet-like nanopillars, which is very different from the circular shape in the previously reported TiN-based VAN structures [20,21,44,45]. To understand the mechanism behind the nanosheet formation, we also investigated the stain states around the nanosheet using geometric phase analysis (GPA) based on a high-resolution STEM (HRSTEM) image. The color maps, ε_{yy} (Fig. 1g) and ε_{xx} (Fig. 1f), are generated with x direction perpendicular to the plate, and y direction parallel to the plate The strain maps are calculated with respect to the lattice plane spacings in the TiN matrix, with a displayed strain ranging from −30% to +30%. A high compressive strain exists in the nanosheet area (i.e., white contrast area) in the ε_{xx} mapping, but a relatively neutral strain (i.e., green contrast) in the nanosheet area in the ε_{yy}. This suggests the higher strain in the x-direction (normal to plate of the pillars) than that in the y-direction (parallel to plate of the pillars). This anisotropic in-plane strain can also explain the anisotropic rectangular shapes of the nanosheets observed which is to minimize the overall strain energy in the entire system, that is, the longer edges present minimal strain (lattice-matched with the TiN matrix), while the shorter edges present large compressive strain to the TiN matrix. The anisotropic in-plane strain can also be confirmed by the intensity line profiles (Fig. S2 b1-b4) extracted from the plan-view HRSTEM image (Fig. 1f). Along the x-direction, the d-spacing of TiN and $CoFe_2$ phase are 2.12 Å and 1.43 Å separately which corresponds with a relatively large lattice strain of 32%. The lattice strain is relatively small along the y-direction because the two phases have comparable d-spacing (2.12 Å for TiN and 2.02 Å for $CoFe_2$). The in-plane orientation relationships can be identified as $CoFe_2$[100]//TiN [200] and $CoFe_2$[011]//TiN [020].

To further investigate the chemical compositions of the TiN–$CoFe_2$ nanocomposites, we conducted X-ray photoelectron spectroscopy (XPS) depth-profiling measurements by alternately sputtering material off the surface and measuring the freshly exposed surface with XPS. Before any sputtering, the surface shows that Fe, Ti, and Co are mostly in the oxide phase, which is expected for films having been exposed to air. It is interesting to note that, as shown in Fig. S3 c-d, after sputtering off the adventitious carbon and oxygen the metallic $CoFe_2$ is revealed to be the dominant species. However, it is noted that the small oxygen peaks remain below the top surface of the nanocomposite sample, which suggests the Co–O and Fe–O bonds remain in the nanocomposites. This is likely due to Co and Fe bonding to oxygen atoms at the nanosheet/matrix interfaces. The XPS shows the coexitance of TiO_xN_y and TiN peaks in Ti 2p spectra in the matrix, indicating minor oxidation of TiN.

The microstructure tunability was realized by tuning laser frequency from 2 Hz to 10 Hz as shown in Fig. 2b and d. Since the $CoFe_2$ nanosheets have a rectangular-shape cross area, we analyzed the length distribution of the short edge and long edge respectively and plotted them in Fig. 2c and f. As laser frequency increases, the dimension of $CoFe_2$ nanosheets decreases significantly. The average dimension of $CoFe_2$ sheets in the 2 Hz sample is $7.39nm \times 30.61nm$,

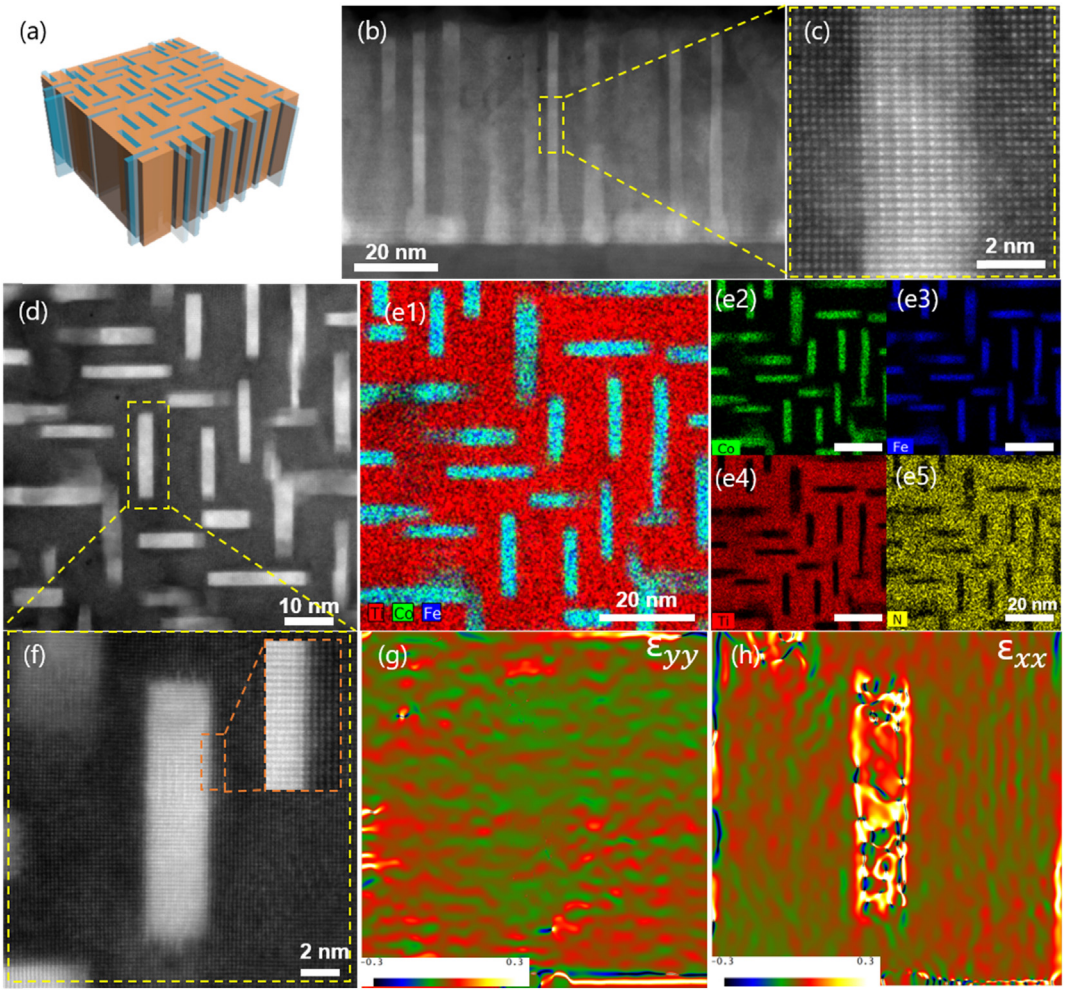

Fig. 1. | Microstructure of TiN–$CoFe_2$ nanocomposite thin film. (a) Schematic drawing of TiN–$CoFe_2$ microstructure; (b) low magnification and (c) high magnification cross-sectional STEM images; (d) plan-view STEM images with (e) corresponding EDS mapping of Co, Fe, Ti, N; (f) high-resolution STEM images of one nanosheet region with ε_{yy} strain mapping (g) and ε_{xx} strain mapping (h). Abbreviations: STEM, scanning transmission electron microscopy; EDS, energy-dispersive X-ray spectroscopy.

while it decreases to $3.14nm \times 16.73nm$ by increasing the laser frequency to 10 Hz. A detailed analysis of the dimension (e.g., maximum, minimum, and mean values) of $CoFe_2$ sheets for all the samples can be found in Supplementary Table S1. The tunability in dimension can be explained by the shorter adatoms diffusion time during the deposition process with higher laser frequency. Besides laser frequency, the temperature-dependent study provides another approach to effectively tune the microstructure of TiN–$CoFe_2$ thin films (Fig. S4). Clearly, as the temperature increases from 500 °C to 700 °C, the $CoFe_2$ nanosheet dimensions increase from $1.45nm \times 4.69nm$ to $7.39nm \times 30.61nm$.

The optical properties of the two-phase TiN–$CoFe_2$ nanocomposites were characterized by spectroscopic ellipsometry. The ellipsometry data ψ and Δ were collected on both 2 Hz and 10 Hz TiN–$CoFe_2$ films and compared with two reference samples, that is, a pure TiN film and a pure $CoFe_2O_4$ film. It is noted the reference single phase $CoFe_2O_4$ film was grown under vacuum condition, which may also have partial reduction and form $CoFe_2$ phase. To retrieve the dielectric permittivity, the data were fitted by applying general oscillator models. The real part of the dielectric permittivity (Fig. 3a) confirms pure TiN is metallic ($\varepsilon' < 0$) and pure $CoFe_2O_4$ film is dielectric ($\varepsilon' > 0$) for most wavelengths. Due to the anisotropic nature of two-phase VAN films, the permittivity of VAN films is fitted and plotted along out-of-plane ($\varepsilon_\perp$) in solid lines and in-plane ($\varepsilon_\parallel$) in dashed lines, respectively. It is clear that the out-of-plane real permittivity ($\varepsilon_\perp$) of both 2 Hz and 10 Hz samples is positive but very close to 0 throughout all the measured wavelengths, while in-plane real permittivity ($\varepsilon_\parallel$) exhibits negative values throughout. The opposite sign in optical permittivity demonstrates a large Type-II hyperbolic dispersion regime (i.e., $\varepsilon_\perp > 0$ and $\varepsilon_\parallel < 0$) as the shaded area in Fig. 3a). Considering the metallic $CoFe_2$, it is possible that the $CoFe_2$ phase could also contribute to the overall negative permittivity in-plane. The remaining small amount of oxygen containing phase at the surface and partial oxidation of TiN matrix near interface could both contribute to the overall positive permittivity out-of-plane. Specifically, based on the effective medium theory for a nanowire system, the effective parallel ($\varepsilon_{xx,yy}$) and perpendicular (ε_{zz}) permittivity values are given by[46]:

$$\varepsilon_{xx,yy} = \frac{\varepsilon_{TiN}[(1+f)\varepsilon_{CF} + (1-f)\varepsilon_{TiN}]}{(1+f)\varepsilon_{TiN} + (1-f)\varepsilon_{CF}}$$

$$\varepsilon_{zz} = f\varepsilon_{CF} + (1-f)\varepsilon_{TiN}$$

where f is the volume fraction of the $CoFe_2$ (CF) nanosheets in the TiN host, ε_{TiN} and ε_{CF} are the permittivity of TiN and $CoFe_2$ phase, respectively. Note that we use the measured permittivity result of TiN film and vacuum growth $CoFe_2O_4$ (CFO) film (shown in Fig. 3a) here for this calculation. The calculated effective permittivity is

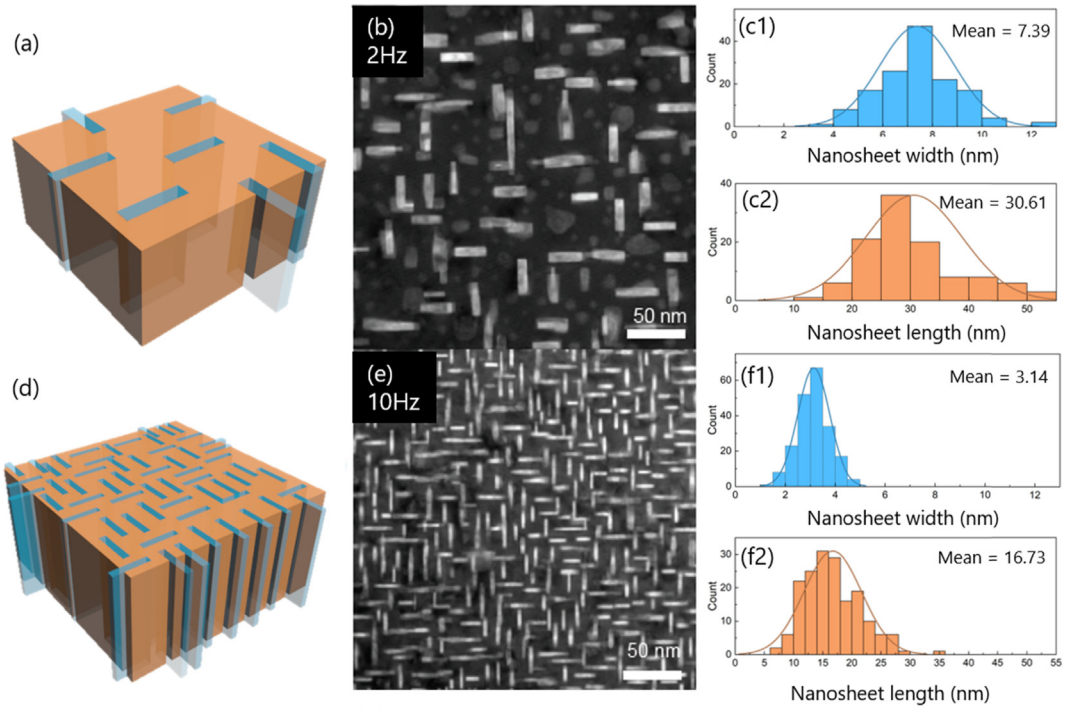

Fig. 2. | Microstructure turnability of TiN–$CoFe_2$ nanocomposite thin films. (a) Schematic drawing of 2 Hz TiN–$CoFe_2$ VAN; (b) plan-view STEM images of 2 Hz TiN–$CoFe_2$ VAN; (c) dimension distribution (short edge width and long edge length) of $CoFe_2$ nanosheets in 2 Hz sample; (d) schematic drawing of 10 Hz TiN–$CoFe_2$ VAN; (e) plan-view STEM images of 10 Hz TiN–$CoFe_2$ VAN; (f) dimension distribution of $CoFe_2$ nanosheets in 10 Hz sample. Abbreviations: STEM, scanning transmission electron microscopy; VAN, vertically aligned nanocomposite.

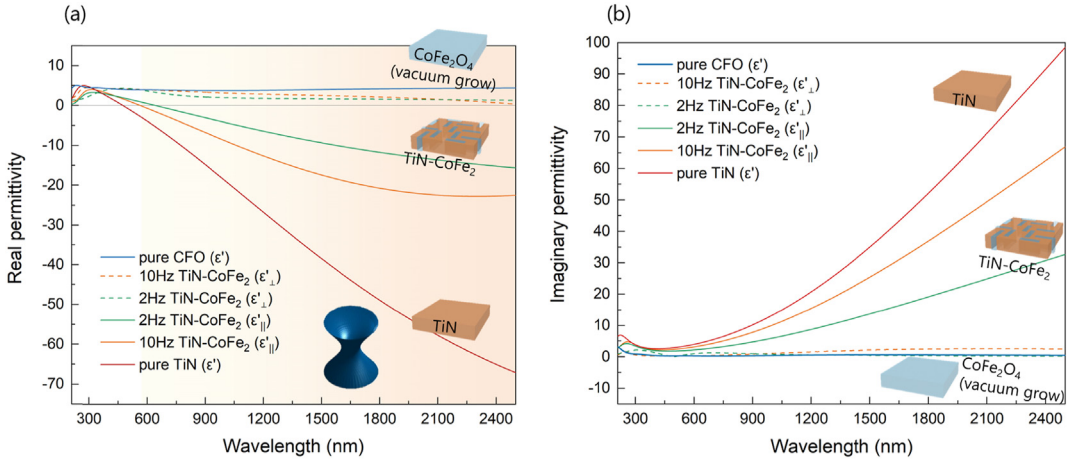

Fig. 3. | Optical properties of TiN–$CoFe_2$ nanocomposite thin films. (a) Real part and (b) imaginary part of permittivity of 2 Hz TiN–$CoFe_2$, 10 Hz TiN–$CoFe_2$, pure TiN, and pure $CoFe_2O_4$ sample.

plotted in Fig. S5. Interestingly, these calculation results show negative ε_{zz} for both samples, which doesn't match very well with the experimental results. The calculation results suggest a metallic behavior in both in-plane and out-of-plane direction, while the experimental results show the samples behave like insulators or dielectric out-of-plane. This discrepancy between the experimental and calculation results is mainly attributed to the remaining oxide phase in the sample. As we discussed above, the X-ray photoelectron spectroscopy (XPS) depth-profiling measurements (Fig. S3) show oxygen-related peaks at the surface as well as in the remaining film. This suggests potential oxide phases remaining in the sample, for example, $CoFe_2O_x$ at the interface between the CF pillars and TiN matrix, which causes the sample to behave less metallic in the perpendicular direction. Note that the 10 Hz sample shows a larger negative value of $\varepsilon'_{||}$ compared to the 2 Hz one, suggesting that higher density of the nanopillars and more vertical interfaces present stronger optical anisotropy in the system. Fig. 3b plots the imaginary permittivity as a function of wavelength. Both the 2 Hz and 10 Hz samples show small optical losses along the out-of-plane direction because of their more dielectric nature compared to the TiN alone. To further explore the plasmonic properties of the film, angular-dependent reflectivity measurements have been conducted on

2 Hz and 10 Hz nanocomposite film and compared with pure TiN and pure $CoFe_2O_4$ samples (Fig. S6). The reflectance spectra of both 2 Hz and 10 Hz nanocomposite samples first reach a minimum at $\lambda \sim 400$ nm then increase as wavelength increases. This observed characteristic of reflectance of the two nanocomposite samples is very similar to that of the pure TiN film with an obvious plasmonic absorption around 400 nm, confirming that our nanocomposite films are plasmonic.

To further study the magnetic behavior of TiN–$CoFe_2$ nanocomposites, magnetization (M) versus magnetic field (H) was measured in in-plane and out-of-plane directions at room temperature using Quantum Design SQUID-VSM. As shown in Fig. 4a, the out-of-plane hysteresis loops of 2 Hz sample exhibits a saturation magnetization $M_{s\perp} = 329\ emu/cm^3$, and coercivity $H_{c\perp} = 1235\ Oe$, while the magnetization and coercivity along in-plane direction are only $M_{s\parallel} = 257\ emu/cm^3$ and $H_{c\parallel} = 708\ Oe$, respectively. The wider out-of-plane loop suggests a strong magnetic anisotropy with an out-of-plane easy axis, which result from the perpendicular elongated shape of $CoFe_2(O)$ nanosheets. The magnetic behavior of 10 Hz sample shows a similar trend, with smaller coercivity $H_{c\perp} = 771\ Oe$ and $H_{c\parallel} = 367\ Oe$ (Fig. 4b). This can be explained by the smaller dimension of $CoFe_2$ nanosheets. Considering the possibility of coupling effect between plasmonic TiN and ferromagnetic $CoFe_2$, it is worth to study their MO coupling properties. Magneto-optic Kerr Effect (MOKE) measurements were conducted on both 2 Hz and 10 Hz samples under room temperature and the results are plotted in Fig. 4c–f. Polar MOKE was measured with a normal incident laser ($\lambda = 632.8\ nm$) and out-of-plane magnetic field, while a 30° laser and in-plane magnetic field were induced in longitudinal MOKE configuration. Due to the limitation of the equipment, the applied field in P-MOKE configuration is in the range of −3500 Oe to 3500 Oe. Therefore, the measured P-MOKE results are weaker than expected since the magnetic moment is not saturated at 3500 Oe. Perpendicular magnetic anisotropy is observed in both samples, which indicates a MO coupling effect. More specifically, the larger P-MOKE signal compared with L-MOKE arises from those vertical TiN/$CoFe_2$ interfaces where the coupling occurs. Furthermore, the 10 Hz sample shows a larger Kerr rotation signal compared to the 2 Hz sample, in both out-of-plane and in-plane directions. This can be explained by the enhanced coupling introduced by the higher

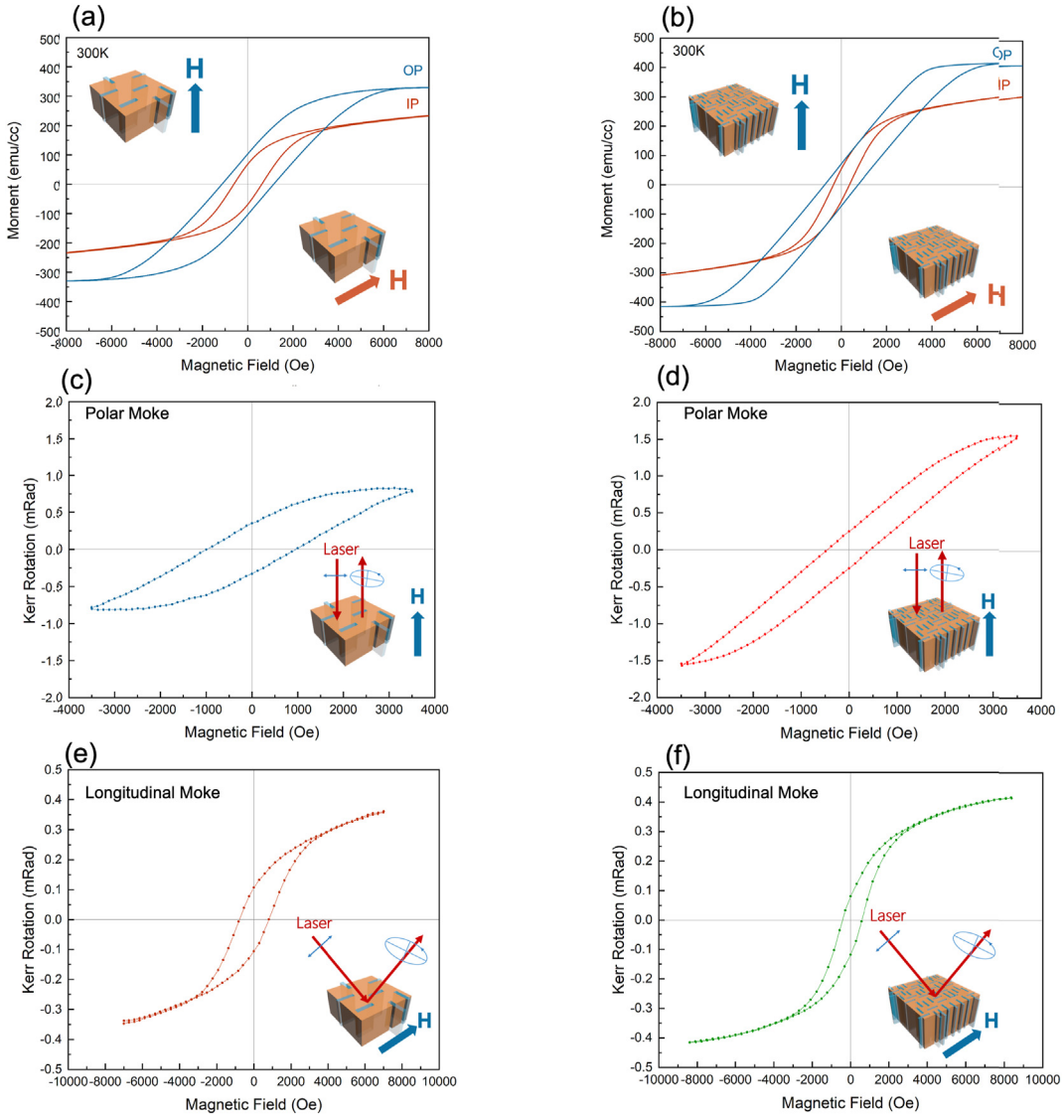

Fig. 4. | Magnetic properties and magneto-optical coupling effect in TiN–$CoFe_2$ nanocomposite thin films. (a) Comparison of in-plane and out-of-plane M – H hysteresis loops of 2 Hz TiN–$CoFe_2$ nanocomposites; (b) comparison of in-plane and out-of-plane M – H hysteresis loops of 10 Hz TiN–$CoFe_2$ nanocomposites; (c) polar and (e) longitudinal Kerr rotation of 2 Hz TiN–$CoFe_2$ nanocomposites; (d) polar and (f) longitudinal Kerr rotation of 10 Hz TiN–$CoFe_2$ nanocomposites.

density of TiN−$CoFe_2$ interfaces in the 10 Hz sample compared to that in the 2 Hz sample. The MO coupling effect has been demonstrated in other TiN-based VANs, such as TiN−NiO [44] and TiN−Fe [47]. Compared with those systems, the MOKE response in this work is much stronger considering the stronger ferromagnetic response of $CoFe_2$.

The overall characteristics of the new TiN−$CoFe_2$ hybrid metamaterial are the anisotropic $CoFe_2$ nanosheets formed in the TiN matrix, high epitaxial film quality, anisotropic optical and magnetic properties, as well as unique MO coupling properties. Compared to the TiN−Au, TiN−Ag, and TaN−Au systems previously demonstrated [19–21], TiN−$CoFe_2$ opens up the potential of highly anisotropic metamaterials designs, that is, hyperbolic dispersion and perpendicular magnetic anisotropy, which can further enhance the MO coupling [48,49]. The unique MO coupling demonstrated at the TiN and $CoFe_2$ interfaces also presents opportunities in future designs of magnetoplasmonic nanostructures toward future light manipulation [50,51]. Most reported magnetoplasmonic nanostructures were fabricated by top-down approaches [49,52,53] including lithography, focused ion-beam milling, or bottom-up approaches [48] for example, template growth, which are tedious. This self-assembled approach allows a simple approach to combine plasmonic and magnetic materials into a nanoscale periodic structure. One of the major challenges is the interdiffusion between the oxide and the nitride in the system and the resultant reduction of the oxide phase. One of the major challenges is the interdiffusion between the oxide and the nitride in the system and the resultant reduction of the oxide phase. Selecting more stable oxides and minimizing interdiffusion by controlling the growth conditions will be critical for future exploration of nitride-oxide hybrid systems. Additional tunability can be achieved by other material combinations, novel three-phase system designs, and multilayer stacks of nitride-oxide VAN with other systems for integrated functionalities.

3. Conclusion

In summary, we have demonstrated self-assembled TiN−$CoFe_2$ nanocomposite thin films by using the one-step PLD technique. Microstructure characterizations by STEM and XPS show ultrathin nanosheets with metallic $CoFe_2$ phase growing vertically aligned in the TiN matrix. Both the deposition frequency study (2 Hz, 10 Hz) and temperature-dependent studies suggest effective tunability in the microstructure of the secondary phase as well as the resultant properties. Ellipsometry measurements reveal that the samples exhibit a Type-II hyperbolic dispersion in most optical wavelengths considering the highly anisotropic morphology of the TiN matrix, vertically aligned metallic $CoFe_2$ nanosheets, and interfacial oxides between the TiN matrix and the $CoFe_2$ nanosheets. The magnetic hysteresis loops reveal magnetic anisotropy owing to the highly aligned $CoFe_2$ nanosheets. The well-integrated plasmonic and ferromagnetic materials in the hybrid system enable a strong MO coupling effect at the pillar−matrix interfaces. This new nitride-based hybrid nanostructures demonstrated in this study effectively combine plasmonic nitride and ferromagnetic $CoFe_2$ toward future magnetic control of optics and potential optical isolation.

4. Methods

4.1. Thin film growth

The TiN−$CoFe_2O_4$ target consists of pie-shape $CoFe_2O_4$ and TiN targets. The nanocomposite thin films were deposited on MgO (001) substrates in Neocera pulsed laser deposition chamber with a KrF excimer laser (Lambda Physik Compex Pro 205, $\lambda = 248$ nm). The substrates were heated and maintained at 700 °C during deposition and a high vacuum condition (2.0×10^{-6} mbar) was kept during deposition and cooling process.

4.2. Structural characterization

4.2.1. X-ray ddiffraction

The $\theta/2\theta$ XRD scans were measured by a Panalytical X'Pert X-ray diffractometer with a Cu Kα1 radiation source ($\lambda = 0.15406$ nm).

4.3. Transmission electron microscopy

Transmission electron microscopy (TEM) and scanning transmission electron microscopy (STEM) (under a high angle annular dark field mode (HAADF)) were taken on a Thermo Fisher Scientific (FEI) Talos F200X system with a point-to-point resolution of 1.6 Å. High-resolution STEM images were collected on an aberration-corrected FEI Titan microscope equipped with a high-brightness Schottky field emission electron source operated at 300 kV. A FEI TitanTM G2 80−200 STEM with a Cs probe corrector and ChemiSTEMTM technology (X-FEGTM and SuperXTM EDS with four windowless silicon drift detectors) operated at 200 kV was used for HAADF-STEM imaging and EDS analysis. A Digital Micrograph plug-in (DM 1.8.3 package, HRTEM Research Inc.) was used for geometric phase analysis (GPA). The cross-sectional TEM samples were prepared by a standard procedure, including manual grinding, polishing, dimpling, and a final ion milling step (PIPS 695 precision ion polishing system, Gatan Inc.).

4.3.1. X-ray photoelectron spectroscopy

XPS was performed using a Kratos Axis Supra XPS system with a monochromatic Al Kα X-ray source. An initial spectrum was taken of the surface of every sample before a depth profile for 40 steps was performed with a gas cluster ion sputtering system at 10 keV 1000 clusters for 60 s with an incidence angle of 40° with respect to the horizontal direction. The size of the analyzed area was 110 μm × 110 μm, while the sputtered size was 2 mm × 2 mm (rastered). Base pressure during analysis was 1.2×10^{-9} torr and the electron emission angle was at 54.7° with an active charge neutralizer. XPS data were analyzed using CasaXPS software with the Kratos relative sensitivity factors set to F 1s at 1. The O 1s signal at 530.6 eV (MgO) was used as an internal reference for peak positions for all samples.

4.4. Optical characterization

Spectroscopic ellipsometry measurements were carried out with a spectroscopic elliposometer (J.A. Woollam RC_2) with variable angles (55°, 65°, and 75°) and spectrum range from 210 nm to 2500 nm. The real and imaginary part of permittivity were obtained by fitting ellipsometer parameters psi (Ψ) and Delta(Δ) with Gen-Osc model in CompleteEASE software. Transmittance spectra were measured on UV−vis−NIR absorption spectrophotometer (Perkin Elmer Lambda 1050).

4.5. Magnetic characterization

The magnetic hysteresis loops were measured by a Quantum Design MPMS-3 SQUID Magnetometer with vibrating sample magnetometer (VSM) mode. The magneto-optic Kerr effect (MOKE) measurements were carried out by a home-built system equipped with a photoelastic modulator with two polar (P) and longitudinal (L) configurations. A laser with a wavelength of 632 nm was applied as a source light and the magnetic field was in the range of −3500 Oe to 3500 Oe for P-MOKE and −7000 Oe to 7000 Oe for L-MOKE separately.

CRediT authorship contribution statement

Jiawei Song: Writing – original draft, Conceptualization, Methodology, Validation, Data curation, Formal analysis, Writing – review and editing, Investigation. **Di Zhang:** Methodology, Investigation, Writing – review and editing. **Ping Lu:** Methodology, Investigation, Writing – review and editing. **Haohan Wang:** Methodology, Investigation, Data curation, Writing – review and editing. **Xiaoshan Xu:** Supervision, Writing – review and editing. **Melissa L. Meyerson:** Methodology, Investigation, Data curation, Writing – review and editing. **Samantha G. Rosenberg:** Methodology, Investigation, Data curation, Writing – review and editing. **Julia Deitz:** Supervision, Writing – review and editing. **Juncheng Liu:** Methodology, Investigation, Writing – review and editing. **Xuejing Wang:** Methodology, Investigation, Writing – review and editing. **Xinghang Zhang:** Supervision, Writing – review and editing. **Haiyan Wang:** Conceptualization, Funding acquisition, Project administration, Resources, Supervision, Writing – review and editing.

Declaration of competing interest

The authors declare that they have no known competing financial interests or personal relationships that could have appeared to influence the work reported in this paper.

Data availability

Data will be made available on request.

Acknowledgment

This work was supported by the U.S. National Science Foundation DMR-2016453 and DMR-1565822 (VAN thin film growth and High-resolution STEM work, respectively). The work at University of Nebraska was supported by the U.S. National Science Foundation through EPSCoR RII Track-1: Emergent Quantum Materials and Technologies (EQUATE), Award No. OIA-2044049. The work at Los Alamos National Laboratory was supported by the NNSA's Laboratory Directed Research and Development Program and was performed, in part, at the Center for Integrated Nanotechnologies, an Office of Science User Facility operated for the U.S. Department of Energy Office of Science. Los Alamos National Laboratory, an affirmative action equal opportunity employer, is managed by Triad National Security, LLC for the U.S. Department of Energy's NNSA, under contract 89233218CNA000001. The microscopy work was partially supported by the Laboratory Directed Research and Development program at Sandia National Laboratories. Sandia National Laboratories is a multi-mission laboratory managed and operated by National Technology and Engineering Solutions of Sandia, LLC., a wholly owned subsidiary of Honeywell International, Inc., for the U.S. Department of Energy's National Nuclear Security Administration under Contract No. DE-NA0003525. This paper describes objective technical results and analysis. Any subjective views or opinions that might be expressed in the paper do not necessarily represent the views of the U.S. Department of Energy or the United States Government.

Appendix A. Supplementary data

Supplementary data to this article can be found online at https://doi.org/10.1016/j.mtnano.2023.100316.

References

[1] D.R. Smith, J.B. Pendry, M.C.K. Wiltshire, Metamaterials and Negative Refractive Index, 2004. https://www.science.org.
[2] V.M. Shalaev, Optical Negative-Index Metamaterials, 2007. www.nature.com/naturephotonics.
[3] N. Kinsey, C. DeVault, A. Boltasseva, V.M. Shalaev, Near-zero-index materials for photonics, Nat. Rev. Mater. 4 (2019) 742–760, https://doi.org/10.1038/s41578-019-0133-0.
[4] A. Poddubny, I. Iorsh, P. Belov, Y. Kivshar, Hyperbolic metamaterials, Nat. Photonics 7 (2013) 958–967, https://doi.org/10.1038/nphoton.2013.243.
[5] P. Shekhar, J. Atkinson, Z. Jacob, Hyperbolic metamaterials: fundamentals and applications, Nano Converg 1 (2014), https://doi.org/10.1186/s40580-014-0014-6.
[6] J.B. Khurgin, A. Boltasseva, Reflecting upon the losses in plasmonics and metamaterials, MRS Bull. 37 (2012) 768–779, https://doi.org/10.1557/mrs.2012.173.
[7] G.v. Naik, V.M. Shalaev, A. Boltasseva, Alternative plasmonic materials: beyond gold and silver, Adv. Mater. 25 (2013) 3264–3294, https://doi.org/10.1002/adma.201205076.
[8] P. Patsalas, N. Kalfagiannis, S. Kassavetis, Optical properties and plasmonic performance of titanium nitride, Materials 8 (2015) 3128–3154, https://doi.org/10.3390/ma8063128.
[9] W.P. Guo, R. Mishra, C.W. Cheng, B.H. Wu, L.J. Chen, M.T. Lin, S. Gwo, Titanium nitride epitaxial films as a plasmonic material platform: alternative to gold, ACS Photonics 6 (2019) 1848–1854, https://doi.org/10.1021/acsphotonics.9b00617.
[10] C.C. Chang, J. Nogan, Z.P. Yang, W.J.M. Kort-Kamp, W. Ross, T.S. Luk, D.A.R. Dalvit, A.K. Azad, H.T. Chen, Highly plasmonic titanium nitride by room-temperature sputtering, Sci. Rep. 9 (2019), https://doi.org/10.1038/s41598-019-51236-3.
[11] T. Krekeler, S.S. Rout, G.v. Krishnamurthy, M. Störmer, M. Arya, A. Ganguly, D.S. Sutherland, S.I. Bozhevolnyi, M. Ritter, K. Pedersen, A.Y. Petrov, M. Eich, M. Chirumamilla, Unprecedented thermal stability of plasmonic titanium nitride films up to 1400 °C, Adv. Opt. Mater. 9 (2021), https://doi.org/10.1002/adom.202100323.
[12] H. Reddy, U. Guler, Z. Kudyshev, A.v. Kildishev, V.M. Shalaev, A. Boltasseva, Temperature-dependent optical properties of plasmonic titanium nitride thin films, ACS Photonics 4 (2017) 1413–1420, https://doi.org/10.1021/acsphotonics.7b00127.
[13] R. Kamakura, S. Murai, S. Ishii, T. Nagao, K. Fujita, K. Tanaka, Plasmonic-photonic hybrid modes excited on a titanium nitride nanoparticle array in the visible region, ACS Photonics 4 (2017) 815–822, https://doi.org/10.1021/acsphotonics.6b00763.
[14] L. Gui, S. Bagheri, N. Strohfeldt, M. Hentschel, C.M. Zgrabik, B. Metzger, H. Linnenbank, E.L. Hu, H. Giessen, Nonlinear refractory plasmonics with titanium nitride nanoantennas, Nano Lett. 16 (2016) 5708–5713, https://doi.org/10.1021/acs.nanolett.6b02376.
[15] E. Shkondin, T. Repän, O. Takayama, A.v. Lavrinenko, High aspect ratio titanium nitride trench structures as plasmonic biosensor, Opt. Mater. Express 7 (2017) 4171, https://doi.org/10.1364/ome.7.004171.
[16] W. Li, U. Guler, N. Kinsey, G.v. Naik, A. Boltasseva, J. Guan, V.M. Shalaev, A.v. Kildishev, Refractory plasmonics with titanium nitride: Broadband, Adv. Mater. 26 (2014) 7959–7965, https://doi.org/10.1002/adma.201401874.
[17] G.v. Naik, B. Saha, J. Liu, S.M. Saber, E.A. Stach, J.M.K. Irudayaraj, T.D. Sands, V.M. Shalaev, A. Boltasseva, Epitaxial superlattices with titanium nitride as a plasmonic component for optical hyperbolic metamaterials, Proc. Natl. Acad. Sci. U. S. A. 111 (2014) 7546–7551, https://doi.org/10.1073/pnas.1319446111.
[18] J. Huang, D. Zhang, H. Wang, Epitaxial TiN/MgO multilayers with ultrathin TiN and MgO layers as hyperbolic metamaterials in visible region, Materials Today Physics 16 (2021), 100316, https://doi.org/10.1016/j.mtphys.2020.100316.
[19] J. Huang, X. Wang, N.L. Hogan, S. Wu, P. Lu, Z. Fan, Y. Dai, B. Zeng, R. Starko-Bowes, J. Jian, H. Wang, L. Li, R.P. Prasankumar, D. Yarotski, M. Sheldon, H.T. Chen, Z. Jacob, X. Zhang, H. Wang, Nanoscale artificial plasmonic lattice in self-assembled vertically aligned nitride–metal hybrid metamaterials, Adv. Sci. 5 (2018), https://doi.org/10.1002/advs.201800416.
[20] X. Wang, J. Jian, S. Diaz-Amaya, C.E. Kumah, P. Lu, J. Huang, D.G. Lim, V.G. Pol, J.P. Youngblood, A. Boltasseva, L.A. Stanciu, D.M. O'carroll, X. Zhang, H. Wang, Hybrid Plasmonic Au-TiN Vertically Aligned Nanocomposites: a Nanoscale Platform towards Tunable Optical Sensing †, 2019, https://doi.org/10.1039/c8na00306h.
[21] X. Wang, J. Jian, Z. Zhou, C. Fan, Y. Dai, L. Li, J. Huang, J. Sun, A. Donohue, P. Bermel, X. Zhang, H.T. Chen, H. Wang, Self-assembled Ag–TiN hybrid plasmonic metamaterial: tailorable tilted nanopillar and optical properties, Adv. Opt. Mater. 7 (2019) 1–9, https://doi.org/10.1002/adom.201801180.
[22] X. Wang, X. Ma, E. Shi, P. Lu, L. Dou, X. Zhang, H. Wang, Large-scale plasmonic hybrid framework with built-in nanohole array as multifunctional optical sensing platforms, Small 16 (2020) 1–10, https://doi.org/10.1002/smll.201906459.
[23] J. Huang, X. Wang, D. Li, T. Jin, P. Lu, D. Zhang, P.T. Lin, H.T. Chen, J. Narayan, X. Zhang, H. Wang, 3D hybrid plasmonic framework with Au nanopillars embedded in nitride multilayers integrated on Si, Adv. Mater. Interfac. 7 (2020) 1–9, https://doi.org/10.1002/admi.202000493.

[24] L. Li, L. Sun, J.S. Gomez-Diaz, N.L. Hogan, P. Lu, F. Khatkhatay, W. Zhang, J. Jian, J. Huang, Q. Su, M. Fan, C. Jacob, J. Li, X. Zhang, Q. Jia, M. Sheldon, A. Alù, X. Li, H. Wang, Self-assembled epitaxial Au-oxide vertically aligned nanocomposites for nanoscale metamaterials, Nano Lett. 16 (2016) 3936–3943, https://doi.org/10.1021/acs.nanolett.6b01575.
[25] J. Huang, X.L. Phuah, L.M. McClintock, P. Padmanabhan, K.S.N. Vikrant, H. Wang, D. Zhang, H. Wang, P. Lu, X. Gao, X. Sun, X. Xu, R. Edwin García, H.T. Chen, X. Zhang, H. Wang, Core-shell metallic alloy nanopillars-in-dielectric hybrid metamaterials with magneto-plasmonic coupling, Mater. Today 51 (2021) 39–47, https://doi.org/10.1016/j.mattod.2021.10.024.
[26] J. Huang, L. Li, P. Lu, Z. Qi, X. Sun, X. Zhang, H. Wang, Self-assembled Co-BaZrO3 nanocomposite thin films with ultra-fine vertically aligned Co nanopillars, Nanoscale 9 (2017) 7970–7976, https://doi.org/10.1039/c7nr01122a.
[27] D. Zhang, Z. Qi, J. Jian, J. Huang, X.L. Phuah, X. Zhang, H. Wang, Thermally stable Au-BaTiO3 nanoscale hybrid metamaterial for high-temperature plasmonic applications, ACS Appl. Nano Mater. 3 (2020) 1431–1437, https://doi.org/10.1021/acsanm.9b02271.
[28] D. Zhang, S. Misra, J. Jian, P. Lu, L. Li, A. Wissel, X. Zhang, H. Wang, Self-assembled BaTiO3-Au xAg1- xLow-loss hybrid plasmonic metamaterials with an ordered "nano-domino-like" microstructure, ACS Appl. Mater. Interfaces 13 (2021) 5390–5398, https://doi.org/10.1021/acsami.0c19108.
[29] J. Lu, R.L. Paldi, Y. Pachaury, D. Zhang, H. Wang, M. Kalaswad, X. Sun, J. Liu, X.L. Phuah, X. Zhang, A.A. El-Azab, H. Wang, Ordered Hybrid Metamaterial of La0.7Sr0.3MnO3-Au Vertically Aligned Nanocomposites Achieved on Templated SrTiO3 Substrate, 2021.
[30] R. Liang, P. Dosanjh, D.A. Bonn, D.J. Baar, J.F. Carolan, W.N. Hardy, Growth and Properties of Superconducting YBCO Single Crystals, 1992.
[31] S.E. Shirsath, X. Liu, Y. Yasukawa, S. Li, A. Morisako, Switching of magnetic easy-axis using crystal orientation for large perpendicular coercivity in CoFe2O4 thin film, Sci. Rep. 6 (2016) 1–11, https://doi.org/10.1038/srep30074.
[32] M. Zheng, X.C. Wu, B.S. Zou, Y.J. Wang, Magnetic Properties of Nanosized MnFe O Particles, 1998.
[33] A. Chen, N. Poudyal, J. Xiong, J.P. Liu, Q. Jia, Modification of structure and magnetic anisotropy of epitaxial CoFe2O4 films by hydrogen reduction, Appl. Phys. Lett. 106 (2015), https://doi.org/10.1063/1.4915504.
[34] C.Y. Kuo, Z. Hu, J.C. Yang, S.C. Liao, Y.L. Huang, R.K. Vasudevan, M.B. Okatan, S. Jesse, S.v. Kalinin, L. Li, H.J. Liu, C.H. Lai, T.W. Pi, S. Agrestini, K. Chen, P. Ohresser, A. Tanaka, L.H. Tjeng, Y.H. Chu, Single-domain multiferroic BiFeO3 films, Nat. Commun. 7 (2016), https://doi.org/10.1038/ncomms12712.
[35] J.M. Moreau, C. Michel, R. Gerson, W.J. James, FERROELECTRIC BiFeO3 X-RAY AND NEUTRON DIFFRACTION STUDY, Pergamon Press, 1971.
[36] B. Zhang, J. Huang, J. Jian, B.X. Rutherford, L. Li, S. Misra, X. Sun, H. Wang, Tuning magnetic anisotropy in Co-BaZrO3 vertically aligned nanocomposites for memory device integration, Nanoscale Adv. 1 (2019) 4450–4458, https://doi.org/10.1039/c9na00438f.
[37] X. Gao, L. Li, J. Jian, H. Wang, M. Fan, J. Huang, X. Wang, H. Wang, Vertically aligned nanocomposite BaTiO3:YMnO3 thin films with room temperature multiferroic properties toward nanoscale memory devices, ACS Appl. Nano Mater. 1 (2018) 2509–2514, https://doi.org/10.1021/acsanm.8b00614.
[38] H. Zheng, J. Wang, S.E. Lofland, Z. Ma, L. Mohaddes-Ardabili, T. Zhao, L. Salamanca-Riba, S.R. Shinde, S.B. Ogale, F. Bai, D. Viehland, Y. Jia, D.G. Schlom, M. Wuttig, A. Roytburd, R. Ramesh, Multiferroic BaTiO3-CoFe2O4 nanostructures, Science 303 (2004) 661–663, https://doi.org/10.1126/science.1094207, 1979.
[39] X. Wang, Z. Qi, J. Liu, H. Wang, X. Xu, X. Zhang, H. Wang, Strong interfacial coupling of tunable Ni–NiO nanocomposite thin films formed by self-decomposition, ACS Appl. Mater. Interfaces (2021), https://doi.org/10.1021/acsami.1c09793.
[40] B. Zhang, M. Kalaswad, B.X. Rutherford, S. Misra, Z. He, H. Wang, Z. Qi, A.E. Wissel, X. Xu, H. Wang, Au-encapsulated Fe nanorods in oxide matrix with tunable magneto-optic coupling properties, ACS Appl. Mater. Interfaces 12 (2020) 51827–51836, https://doi.org/10.1021/acsami.0c14424.
[41] D.A.M.J.L.G.P.H.C.H.-J.L.G. P. M. Voyles*, Atomic-scale Imaging of Individualdopant Atoms and Clusters in Highlyn-type Bulk Si, (n.d.).
[42] R. Erni, H. Heinrich, G.Z. Kostorz Eth, Quantitative Characterisation of Chemical Inhomogeneities in Al-Ag Using High-Resolution Z-Contrast STEM, 2003.
[43] D.O. Klenov, S. Stemmer, Contributions to the contrast in experimental high-angle annular dark-field images, Ultramicroscopy 106 (2006) 889–901, https://doi.org/10.1016/j.ultramic.2006.03.007.
[44] X. Wang, H. Wang, J. Jian, B.X. Rutherford, X. Gao, X. Xu, X. Zhang, H. Wang, Metal-free oxide-nitride heterostructure as a tunable hyperbolic metamaterial platform, Nano Lett. 20 (2020) 6614–6622, https://doi.org/10.1021/acs.nanolett.0c02440.
[45] X. Wang, X. Ma, E. Shi, P. Lu, L. Dou, X. Zhang, H. Wang, Large-scale plasmonic hybrid framework with built-in nanohole array as multifunctional optical sensing platforms, Small 16 (2020) 1–10, https://doi.org/10.1002/smll.201906459.
[46] Prashant Shekhar, Jonathan Atkinson, Zubin Jacob, Hyperbolic metamaterials: fundamentals and applications, Nanoconvergence (2014) 1–14, https://doi.org/10.1186/1687-6180-2011-78.
[47] M. Kalaswad, D. Zhang, B.X. Rutherford, J. Lu, J.P. Barnard, Z. He, J. Liu, H. Wang, X. Xu, H. Wang, TiN–Fe vertically aligned nanocomposites integrated on silicon as a multifunctional platform toward device applications, Crystals 12 (2022), https://doi.org/10.3390/cryst12060849.
[48] I.v. Malysheva, I.A. Kolmychek, A.M. Romashkina, A.P. Leontiev, K.S. Napolskii, T.v. Murzina, Magneto-optical effects in hyperbolic metamaterials based on ordered arrays of bisegmented gold/nickel nanorods, Nanotechnology 32 (2021), https://doi.org/10.1088/1361-6528/abf691.
[49] J. Kuttruff, A. Gabbani, G. Petrucci, Y. Zhao, M. Iarossi, E. Pedrueza-Villalmanzo, A. Dmitriev, A. Parracino, G. Strangi, F. de Angelis, D. Brida, F. Pineider, N. Maccaferri, Magneto-optical activity in nonmagnetic hyperbolic nanoparticles, Phys. Rev. Lett. 127 (2021), https://doi.org/10.1103/PhysRevLett.127.217402.
[50] N. Maccaferri, I. Zubritskaya, I. Razdolski, I.A. Chioar, V. Belotelov, V. Kapaklis, P.M. Oppeneer, A. Dmitriev, Nanoscale magnetophotonics, J. Appl. Phys. 127 (2020), https://doi.org/10.1063/1.5100826.
[51] C. Rizal, M.G. Manera, D.O. Ignatyeva, J.R. Mejía-Salazar, R. Rella, V.I. Belotelov, F. Pineider, N. MacCaferri, Magnetophotonics for sensing and magnetometry toward industrial applications, J. Appl. Phys. 130 (2021), https://doi.org/10.1063/5.0072884.
[52] R.M. Rowan-Robinson, J. Hurst, A. Ciuciulkaite, I.-A. Chioar, M. Pohlit, M. Zapata-Herrera, P. Vavassori, A. Dmitriev, P.M. Oppeneer, V. Kapaklis, Direction-sensitive magnetophotonic surface crystals, Adv Photonics Res 2 (2021), 2100119, https://doi.org/10.1002/adpr.202100119.
[53] G. Petrucci, A. Gabbani, I. Faniayeu, E. Pedrueza-Villalmanzo, G. Cucinotta, M. Atzori, A. Dmitriev, F. Pineider, Macroscopic magneto-chiroptical metasurfaces, Appl. Phys. Lett. 118 (2021), 251108, https://doi.org/10.1063/5.0050797.